Special Collection

Oxygen Reduction Reaction at Single-Site Catalysts: A Combined Electrochemical Scanning Tunnelling Microscopy and DFT Investigation on Iron Octaethylporphyrin Chloride on HOPG**

Alessandro Facchin,[a] Mirco Zerbetto,[a] Armando Gennaro,[a] Andrea Vittadini,[a, b] Daniel Forrer,[a, b] and Christian Durante*[a]

Here, we investigate the electrochemical activity of a highly oriented pyrolytic graphite (HOPG) supported iron octaethylporphyrin chloride film as a working electrode for the oxygen reduction reaction in 0.1 M $HClO_4$ electrolyte. A voltammetric investigation indicated a quasi-reversible electron transfer for the Fe^{III}/Fe^{II} redox process, which turned out to be responsible for a "redox catalysis like" mechanism, in which the reduction of the metal center is first required to allow the O_2 reduction. Here we proved that O_2 is mostly reduced to H_2O in a tetraelectronic process, as evidenced by a rotating ring-disk electrode (RRDE). Furthermore, electrochemical scanning tunnelling microscopy (EC-STM) is used as in *operando* technique for probing the electrode surface at the atomic level while the oxygen reduction reaction occurs, obtaining information on the molecule adlayer electronic and topographic structures. This allows us to follow the change in redox state from Fe^{III} to Fe^{II} induced by the change of the electrode potential in O_2 saturated electrolyte. The adsorption of O_2 at the iron center was visualized and its depletion upon the application of a potential at which O_2 can be reduced. The ORR process catalyzed by FeOEP adsorbed on HOPG was modelled by combining density functional theory, molecular dynamics, and thermodynamics data.

1. Introduction

Molecular systems able at mimic biological processes like photosynthesis are of primary importance for understanding the fundamental effects occurring in single site atom catalysts (SAC), which are recently emerging as a new frontier in catalysis science, especially when the active site is a metal atom.[1] With maximum atom-utilization efficiency and unique properties, SACs exhibit great potential for enabling reasonable use of metal resources and achieving atomic economy.[2] Single metal atoms are strongly stabilized by donors such as N atoms, which are present in carbon materials in the form, among others, of pyridinic or pyrrolic functional groups. Nitrogen atoms not only strongly anchor individual metal centres but also modify the electronic properties of the carbon material, thus altering the

catalytic activity. Ternary M−N−C materials (where, for example, M≡Co or Fe), which feature atomically dispersed M centres bonded to neighbouring N atoms, have been intensely investigated as promising candidates to replace Pt in a variety of electrocatalytic reactions, such as the O_2 and CO_2 reduction reactions.[3–6] Notwithstanding the high research interest, atomically dispersed M−N−C materials have been systematically synthetized and investigated only very recently. Actually, the development of the concept of SACs has coincided with recent advances in atomic-resolution characterization techniques, such as high-angle annular dark-field scanning transmission electron microscopy and extended X-ray absorption fine structure, along with theoretical modelling.[7,8] However, neither the synthesis of M−N−C materials nor the structural identification of their M−N_x sites is a trivial task. In fact, even though there is a general consensus on the capability of M−N_x sites to play as catalytic sites for many reactions of interest in modern electrocatalysis, there is still a lack of knowledge about the shape of the active site, and on the properties which govern the catalytic activity and selectivity. Thus, it becomes necessary to make use of complementary techniques to assess whether M−N_x is indeed the active site or simply a co-active site. Knowing the precise active site(s) holds a primary role for the determination of the reaction mechanism. For example, the oxygen reduction reaction (ORR) is known to proceed through a $2e^-$ or $4e^-$ pathway. Understanding which of the two mechanisms predominates would allow to design more performing catalysts avoiding the formation of H_2O_2, which is harmful for a Nafion-based membrane in a low temperature fuel cell. Conversely, the ability to selectively drive the ORR reaction to H_2O_2 opens new

[a] A. Facchin, Prof. M. Zerbetto, Prof. A. Gennaro, Dr. A. Vittadini, Dr. D. Forrer, Prof. C. Durante
Department of Chemical Sciences
University of Padova
via Marzolo 1, 35131, Padova, Italy
E-mail: Christian.durante@unipd.it

[b] Dr. A. Vittadini, Dr. D. Forrer
Istituto di Chimica della Materia Condensata e di Tecnologie per l'Energia ICMATE-CNR
via Marzolo 1, I-35131 Padova, Italy

[**] HOPG: Highly Oriented Pyrolytic Graphite

perspectives in the production of hydrogen peroxide market, which is extensively used as a bleaching agent in the paper and pulp industry.[9–11]

Metal phthalocyanines[12] and porphyrins[13] are known to act as catalysts for O_2 or CO_2 reduction since 1960's and are indeed good model systems for mimicking M–N_4 sites present in carbon materials.[14] Therefore, it becomes obvious that we can use them as model systems to describe how the catalytic activity of M–N_x centres can be affected by metal type, ancillary functionalization, and type of electrode support. These macrocyclic molecules can be used as precursors in the synthesis of M–N–C, or be deposited from a solution phase on a support. If the support is a single crystal, a highly ordered surface also suitable for self-assembly characterisation is obtained. Furthermore, if the substrate is a conductor, the molecular system can be characterized in a typical three electrodes electrochemical cell for standard electrochemical measurements or even probed by means of electrochemical scanning tunnelling microscopy (EC-STM).[12,13,15] In fact, EC-STM allows to characterise molecules adsorbed on the electrode surface and it is potentially a powerful tool to study single site metal catalysts at nanoscopic level. Actually, EC-STM can be regarded as an *in operando* technique since the substrate electrode can be polarised at convenient potentials, purposely determined on the basis of cyclic voltammetry analysis, and corresponding images can be obtained by EC-STM. Therefore, all the electrochemical processes (change in redox states) and the subsequent phenomena such as the surface coverage and molecules orientation can be induced by the applied potential. Furthermore, EC-STM can, in principle, detect (by applying proper potentials) the adsorption, reduction and desorption processes at the M–N_4 site of O_2 eventually present in solution.[12,16,17] In this paper we characterize the structure and the reactivity of an iron octaethylporphyrin film supported on a HOPG surface using a combined approach based on EC-STM. The aim is to understand how the active site evolves during the oxygen reduction process in acidic electrolyte. Iron porphyrin derived catalysts are commonly characterized in alkaline electrolyte, because of a major stability. However, the boom of carbon based materials bearing Fe–N_x active sites have prompted the investigation in acidic electrolyte, where these catalysts are considered to be promising to overcome Pt based catalysts in PEM fuel cells.

2. Results and Discussion

We first consider the functionalization of HOPG by the probe molecules octaethylporphyrin and iron octaethylporphyrin chloride: the two adlayers were tested in 0.1 M $HClO_4$. The free-base porphyrin allows to evaluate any possible physical chemical phenomenon involving the ligand alone, without the presence of iron. For this reason, HOPG was functionalised with pure H_2OEP, obtaining large ordered domains without significant defects, as shown in Figure 1a and 1a'. This indicates that the ligand itself contains functional groups able to enhance the adsorption stability, as well as the diffusion barrier, in all directions within the basal plane, immobilizing the molecules on the HOPG substrate.[18,19] The image was analysed, and unit
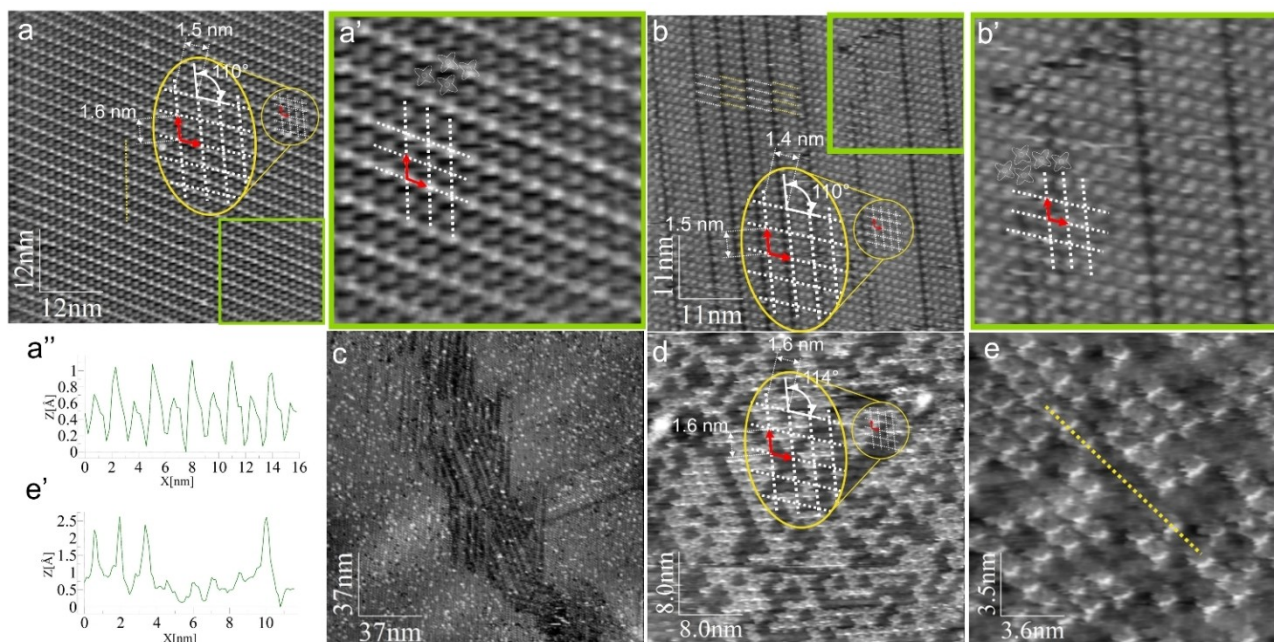

Figure 1. EC-STM in 0.1 M $HClO_4$ of (a) H_2OEP@HOPG $I_t = 0.70$ nA; $U_b = -600$ mV; $E_{app} = 550$ mV vs. RHE; $I = 0$ μA; (a') magnified portion of Figure 1a with stylized shapes of the molecules (a'') topographic profile along the yellow dashed line in figure 1a; (b,c) FeOEP@HOPG at different magnification (b) $I_t = 0.58$ nA; $U_b = -450$ mV; $E_{app} = 650$ mV vs. RHE; $I = 0$ μA, (b') magnified portion of Figure 1b with stylized shapes of the molecules (c) $I_t = 0.58$ nA; $U_b = -650$ mV; $E_{app} = $ OCP. (d,e) EC-STM in 0.1 M $HClO_4$ of a mixed $H_2OEP + FeOEP$ adlayer, (d) $I_t = 0.58$ nA; $U_b = -500$ mV; $E_{app} = $ OCP; $I = 0$ μA, (e) $I_t = 0.86$ nA; $U_b = -550$ mV; $E_{app} = $ OCP; $I = 0$ μA. (e') topographic profile along the yellow dashed line in figure 1e. In figure a,b and d, the greater yellow ellipse magnifies the part bordered by the smaller circle that defines the cell unit.

ChemElectroChem

Articles
doi.org/10.1002/celc.202100543

Chemistry Europe
European Chemical
Societies Publishing

cell parameters were determined, as sketched in Figure 1a and 1a' (the cell unit is delimited by the small yellow circle and magnified in the yellow ellipse). The unit cell vectors are $a_1 = (1.5 \pm 0.1)$ nm, $a_2 = (1.5 \pm 0.1)$ nm, the angle is $\alpha = (112 \pm 2)°$, the surface concentration is $5.13 \cdot 10^{13}$ molecule cm^{-2} and the corresponding surface coverage is $\theta = 0.027$. The adlayer was found to be highly ordered and almost no defects were encountered. However, molecular rows are arranged with an alternating height, as shown in the topographic profile extracted along the yellow dashed line (Figure 1a''). These modulations are limited to the height range between 0.6 Å and 0.8 Å. This effect is generated by the ethyl peripheral substituents, which are free to rotate around their σ bonds and adjust their positions to optimise the molecular packing.

The FeOEP adlayer was found to be more defective than the free-based parent H$_2$OEP. In fact, many domain boundaries are visible (Figure 1b and 1b'). Though each domain is large enough to contain more than 100 molecules, larger defective areas are also found, as shown in (Figure 1c). Unit cell parameters were evaluated and sketched in (Figure 1b), resulting in $a_1 = (1.4 \pm 0.1)$ nm, $a_2 = (1.5 \pm 0.1)$ nm, $\alpha = (110 \pm 2)°$, the surface concentration is $5.50 \cdot 10^{13}$ molecule cm^{-2} and the surface coverage is $\theta = 0.029$. For both H$_2$OEP and FeOEP, the angle between the two unit cell vectors was found to be close to 120°, pointing out a substrate template effect on the growing adlayer during the functionalisation procedure.

The supported FeOEP monolayer was investigated also by means of DFT calculations. We first devised a model able to reproduce the experimental surface cell. To this end, we tested five supercells whose structure reproduces the observed cell within a ± 1 Å and $\pm 5°$ tolerance (Figure 2). For each of them, adsorption energies were computed according to equation:

$$E_{ads} = E_{DFT}^{Fe^{III}ClOEP@HOPG} - \left(E_{DFT}^{Fe^{III}ClOEP} + E_{DFT}^{HOPG} \right) \quad (1)$$

where $E_{DFT}^{Fe^{III}ClOEP@HOPG}$ is the total energy of the HOPG-supported FeClOEP, while $E_{DFT}^{Fe^{III}ClOEP}$ and E_{DFT}^{HOPG} are the total energies of the isolated molecule and of the HOPG slab, respectively. In all cases the molecule was placed with the Fe atom on top of a C atom of the HOPG surface.

We found that the denser surface model $\begin{pmatrix} 4 & -2 \\ 3 & 7 \end{pmatrix}$, with $a_1 = 13.05$ Å, $a_2 = 15.00$ Å and $\alpha = 114°$, is clearly favoured over all of the other options (Table 1). This supercell was then used to compare the adsorption of FeClOEP at three HOPG sites: on-top of a surface atom, at a hollow site, i.e. over the centre of a carbon ring, and at a bridge site. Small differences in adsorption energies were found. In particular, the on-top configuration and the bridge differ by less than 0.01 eV, while the hollow configuration is less stable by 0.1 eV. A configuration where the adsorbate Cl atom is pointing towards a hollow site was found to be 1.1 eV less stable.

It is worth to note that the catalytic species for the ORR is Fe^{II}OEP, and therefore the Fe^{III}ClOEP molecule must lose the chloride ion to be activated. To check whether the chloride ion
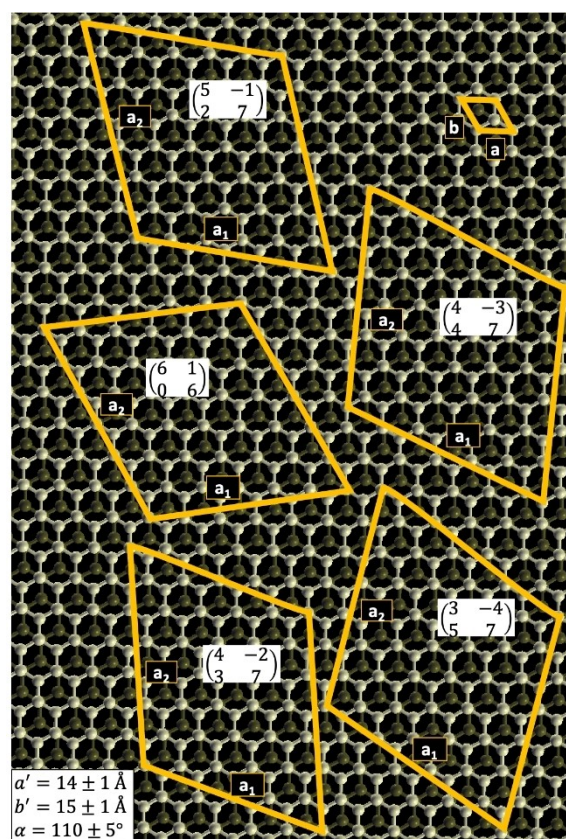

Figure 2. Graphite (0 0 1) surface, 5 model supercells are reported.

Table 1. Adsorption energies E_{ads} of FeClOEP on an on-top site of the HOPG surface of overlayer models. Surface areas and adsorption energy densities per surface area (ϵ_{ads}) are also reported.

Model	Surface area [Å^2]	E_{ads} [eV]	ϵ_{ads} [meV Å^{-2}]
$\begin{pmatrix} 3 & -4 \\ 5 & 7 \end{pmatrix}$	215.2	−2.91	−13.51
$\begin{pmatrix} 4 & -3 \\ 4 & 7 \end{pmatrix}$	210.0	−2.88	−13.70
$\begin{pmatrix} 5 & -1 \\ 2 & 7 \end{pmatrix}$	194.2	−2.82	−14.50
$\begin{pmatrix} 6 & 1 \\ 0 & 6 \end{pmatrix}$	189.0	−2.85	−15.07
$\begin{pmatrix} 4 & -2 \\ 3 & 7 \end{pmatrix}$	178.5	−3.00	−16.80

is readily lost in the as-deposited monolayer or it rather detaches from the Fe centre during the potential scan, we modelled the substitution of the chloride ion with a water molecule by means of DFT calculations on the supported porphyrin. We consider the process:

$$Fe^{III}ClOEP + e^- + H_2O \rightarrow Fe^{II}OEP(H_2O) + Cl^- \quad (2)$$

because the stable oxidation state of iron in solution is Fe^{II}.

The energy variation associated to reaction (2) was computed as:

$$\Delta E = \Delta E_{DFT} + E_{solv}(Cl^-) - E_{solv}(H_2O) + e\varphi \qquad (3)$$

where ΔE_{DFT} is the energy difference between products and reactants computed at the DFT level, solvation energy $E_{solv}(Cl^-)$ is taken from Ref. [20], and the opposite of vaporization enthalpy of water ($\Delta H_{vap} = 40.8$ kJ mol^{-1}) was used as its solvation energy $E_{solv}(H_2O)$. At the absolute potential of the Hydrogen Standard Electrode 4.44 V, $\Delta E = -62.3$ kJ mol^{-1}, and thus the formation of the active species is energetically favoured. Computational outcomes show that the loss of the chloride ion happens in the deposition stage, and therefore the as-deposited monolayer is composed by Fe^{II}OEP molecules.

Moreover, when FeOEP units are considered in place of FeClOEP, the bridge site is destabilized, and its total energy becomes 0.08 eV larger than the on-top one. The hollow configuration remains the least favoured with a total energy larger than the on-top site by 0.17 eV. In the following, iron-containing porphyrin layers are treated as composed by FeOEP units adsorbed flat on HOPG with the Fe atom placed on top of surface C.

In order to bring out the differences between H$_2$OEP and FeOEP and to clarify the existence and the role of the molecule-molecule and molecule-substrate interactions, a mixed layer of the two porphyrins was evaluated (Figure 1d,e). Even if the two pure components were studied, their combination is expected to produce different properties of the adlayer, for which it is worth to conduct EC-STM experiments. It is worth noting that the two porphyrins domains are still well distinguishable at the solid/electrolyte interface, but the adlayer morphologies result different from those of the single systems, even if the ligand is the same. It appears that the number of defects is smaller than the respective pure FeOEP porphyrins adlayer. Furthermore, the typical domain boundaries of FeOEP were not visualised, as well as the surface modulations of H$_2$OEP (Figure 1d). At a first sight, the two components appear randomly distributed, but they tend to not mix with each other, preferring to organise in small pure 2D clusters surrounded by pure 2D clusters of the other species. Only short rows of alternated molecules are present (Figure 1e). The topographic profile running along the yellow dashed line of Figure 1e was extracted and reported in Figure 1e'. The H$_2$OEP molecules are darker in the image and they feature a smaller protrusion than FeOEP in the topographic profile, which is however negligible if compared to the protrusions ascribed to FeOEP ($\Delta Z \approx 1.5$ Å).

FeOEP@HOPG functionalized electrode was investigated by cyclic voltammetry in argon purged 0.1 M HClO$_4$ electrolyte; the comparison between bare HOPG and FeOEP@HOPG electrodes is reported in Figure 3a. CVs were collected with fresh samples, trying to collect the least number of CV as possible, in order to exclude the effect of the degradation of the sample. HOPG ($\varnothing = 4$ mm) does not show any particular feature in cathodic direction in pure electrolyte except for the increasing current recorded in the limit of hydrogen evolution reaction (HER). In the opposite direction (not reported) a flat background attests the absence of any faradaic processes for the exception of oxygen evolution reaction (OER). Conversely, CV for FeOE-
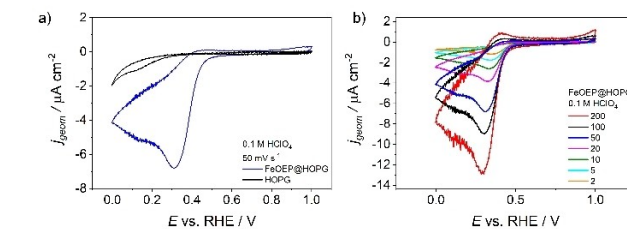

Figure 3. a) CVs of HOPG (black line) and FeOEP@HOPG (blue line) electrodes in Ar purged 0.1 M HClO$_4$ recorded at 0.05 V s^{-1}, b) FeOEP@HOPG electrodes in Ar purged 0.1 M HClO$_4$ recorded at different scan rates (values reported in the Figure are in V s^{-1}).

P@HOPG, recorded at 50 mV s^{-1}, shows a well defined reduction peak with $E_p = 0.315$ V, which is partially reversible as confirmed by the presence of a small anodic counterpart picked at $E_p = 0.40$ V. Based on the observed CVs and previous reports, the reversible pair of peaks with $E_{p,c} = 0.315$ V and $E_{p,a} = 0.400$ V vs. RHE can be assigned to the first one-electron transfer step resulting in a reduction/oxidation of the central iron atom from Fe^{III}OEP to Fe^{II}OEP and vice versa.[21–24]

It is worth noting that the reversibility for the Fe^{III}/Fe^{II} process increases by increasing the scan rate (Figure 3b). The low stability of the FeOEP adlayer prevented a comprehensive investigation of the electron transfer process. However, the partial reversibility can be explained by considering an EC mechanism, i.e. an electron transfer followed by a chemical reaction, such as the reaction with O$_2$ that might be present as contamination even after extensive Ar purging.

When the scan rate is increased, the Fe^{III}/Fe^{II} process becomes more reversible (appearance of a more pronounced anodic counterpart, even if the full reversibility was not reached in the adopted scan rate range), meaning that possible chemical follow ups are hindered in the time scale of the cyclic voltammetry. Figure 4a reports the comparison of the electro-chemical behaviour of bare HOPG, FeOEP@HOPG and
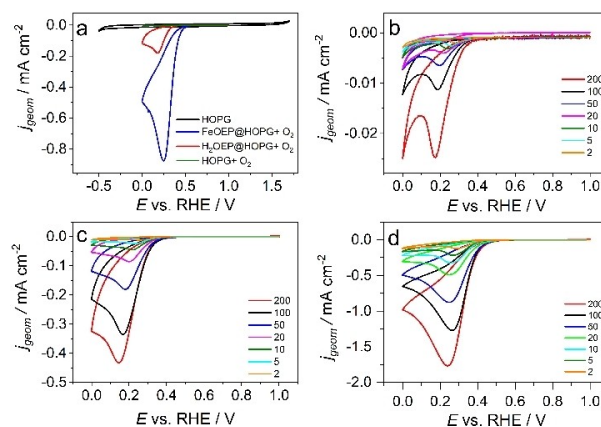

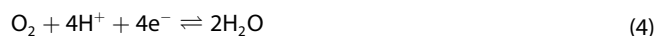**Figure 4.** a) cyclic voltammetry in O$_2$ saturated 0.1 M HClO$_4$ recorded at 0.05 V s^{-1} of HOPG (green line, barely visible), H$_2$OEP@HOPG (red line) and FeOEP@HOPG (blue line) electrodes, HOPG (black line) in Ar purged electrolyte is also reported. CV of O$_2$ reduction in 0.1 M HClO$_4$ at different scan rate at b) HOPG, c) H$_2$OEP@HOPG and d) FeOEP@HOPG.

ChemElectroChem

Articles
doi.org/10.1002/celc.202100543

**Chemistry
Europe**
European Chemical
Societies Publishing

$H_2OEP@HOPG$ in O_2 saturated electrolyte. It is obvious that HOPG has no clear activity for the O_2 reduction in the same investigation range of porphyrins, whereas both H_2OEP and FeOEP showed to have, even if at different extent. In fact, ORR at FeOEP@HOPG results in a very intense reduction peak, where the integrated charge is five times larger than that for the O_2 reduction at $H_2OEP@HOPG$. Furthermore, E_p at FeOEP@HOPG is 70 mV more positive than that recorded on $H_2OEP@HOPG$ electrode, attesting a superior catalytic activity for the meta-lated porphyrin with respect to the non-metalated one. Figures 4b-d report the CVs at different scan rates for the three cases: HOPG, $H_2OEP@HOPG$ and FeOEP@HOPG. The O_2 current at HOPG is clearly very low with respect $H_2OEP@HOPG$ and the comparison is even more striking in the case of FeOEP@HOPG. Furthermore, it is interesting to observe that the E_p for the ORR process is very similar at HOPG and $H_2OEP@HOPG$. To the best of our knowledge there are no literature investigations on supported or unsupported metal free porphyrins active for ORR. Therefore, this is the first example of H_2OEP supported on an electrode showing activity versus ORR. It was recently reported in literature that 2,2′-Dipyridylamine supported on glassy carbon is able to catalyse O_2 reduction in H_2SO_4.[25] In that paper the authors show by DFT calculations that the pyridyl- and amino-N play as the anchoring sites for the ORR reaction intermediates. On the other hand, several authors showed by DFT calculations that O_2 can get adsorbed and reduced favourably on the ortho-C atom of the pyridinic ring.[26–29] It is well established that nitrogen functional groups are capable of increasing ORR catalytic activity in various types of carbon supports.[9–11,30,31] Therefore it may be assumed that the pyrrolic moiety can promote the adsorption and reduction of oxygen directly on nitrogen atoms or on the nearby carbons atoms.[32]

Yin et al.[25] pointed also out that 2,2′-Dipyridylamine has high selectivity versus the reduction of O_2 to H_2O_2.

In fact, it is well known that the reduction process can proceed according to a four electrons pathway (eq. 4) or by two bielectronic steps (eq. 5–6)

$$O_2 + 4H^+ + 4e^- \rightleftharpoons 2H_2O \tag{4}$$

$$O_2 + 2H^+ + 2e^- \rightleftharpoons H_2O_2 \tag{5}$$

$$H_2O_2 + 2H^+ + 2e^- \rightleftharpoons 2H_2O \tag{6}$$

Following the Yin et al. example, we supported both H_2OEP and FeOEP on the GC disk of a RRDE electrode and tested both molecule in an O_2 saturated $HClO_4$ electrolyte (Figure 5). Being HOPG and GC both inert carbon materials we are not expecting important differences in switching from one to the other as evidenced by the cyclic voltammetry response. Differently from 2,2′-Dipyridylamine, FeOEP@GC showed an almost four electron reduction process of O_2 to H_2O (Figure 5c), whereas the competitive mechanism to H_2O_2 becomes more effective at $H_2OEP@GC$ even if the tetraelectronic mechanism is still the most prominent (Figure 5d).

Tylus et al. describe the tetraelectronic reduction of O_2 in Fe–N–C catalysts in acid electrolyte as a $2+2$ electron process
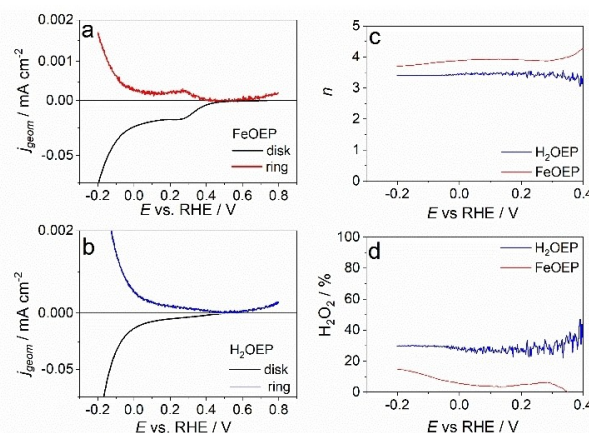

Figure 5. RRDE polarization curves of a) FeOEP@GC and b) $H_2OEP@GC$ in O_2 saturated 0.1 M $HClO_4$; rotation rate 1600 rpm, scan rate 5 mV s^{-1}; c) number of exchanged electrons and d) H_2O_2 yield determined by RRDE experiment.

where the Fe–N_x site is involved in the initial 2e$^-$ reduction to peroxide intermediate, which needs a secondary active sites, situated at close proximity to the primary Fe–N_4 centre to ensure the subsequent reduction to the 4e$^-$ product.[33] The only other active site present in FeOEP adlayer is the porphyrin ligand itself and in particular the pyrrolic nitrogen or the carbon atoms close to the nitrogen functionality. Artyushkova et al. also report that Fe–N_x sites either reduces oxygen to water directly via 4e$^-$ reaction or reduces hydrogen peroxide to water.[34] Therefore it can be inferred that the reduction mechanism of O_2 at FeOEP adlayer occurs via 4 e$^-$ or via $2+2$ e$^-$ at the iron site, with a possible cooperation of the porphin ligand, which showed an activity versus ORR. However, Gibbs free energy calculations discussed later in the text show that the four electrons pathway is preferred over the formation of the H_2O_2 intermediate. To get a deeper understanding of ORR process we employed EC-STM, which allows to evaluate any possible physical chemical phenomenon occurring on the molecules as a function of time or applied potential.

The general procedure consists first in the evaluation of the stability and of the structuration of the molecular adlayer on the HOPG surface at the pH of the electrolytic solution saturated with O_2. In the second case, potentiodynamic imaging is operated, meaning that a precise electrode potential is applied to the HOPG support, which is experienced by the molecular adlayer deposited on it. Upon variation of the applied potential, the electrified interface can undergo changes such as adsorption or desorption of O_2, which can be probed by EC-STM. For all the measured samples, the starting applied potential was close to the OCP, in order to avoid any significant phenomenon on the macrocyclic molecules. The potential was then stepped in cathodic direction since these potentials were revealed by CV to trigger the oxygen reduction reaction (Figure 4).

In the case of an adlayer of pure H_2OEP in contact with O_2 saturated 0.1 M $HClO_4$, the starting applied potential was $E_{app} = 0.55$ V vs. RHE (Figure 6a). At this potential, each molecule is properly resolved, and a cavity at the centre appears from the
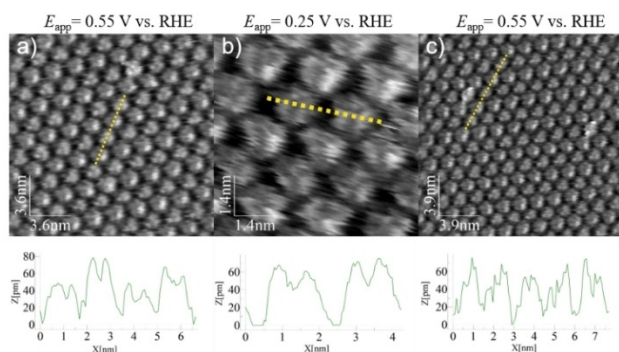
ChemElectroChem

Articles
doi.org/10.1002/celc.202100543

Chemistry
Europe
European Chemical
Societies Publishing

Figure 6. EC-STM of H$_2$OEP@HOPG in O$_2$ saturated 0.1 M HClO$_4$ $I_t = 0.72$ nA; $U_b = -0.900$ V vs. RHE; a) $E_{app} = 0.55$ V vs. RHE; $I = 0$ μA; b) $E_{app} = 0.25$ V vs. RHE; $I = -0.9$ μA; c) $E_{app} = 0.55$ V vs. RHE; $I = 0$ μA; the underneath topographic profile are traced along the yellow dashed line in the corresponding figures (a-c).

topographic profile reported under each figure. This is in accordance with the molecular structure since no metals are accommodated inside the cavity.

The potential was then stepped to $E_{app} = 0.25$ V vs. RHE, which is close to the E_p revealed by CV (Figure 4c). Even at such potentials the H$_2$OEP adlayer retained its stability at the surface, and molecules were properly resolved (Figure 6b). The cavity was again observed, and the general contrast of each molecule did not change, indicating the O$_2$ is not adsorbing on the centre of the molecules. By sweeping the potential back to $E_{app} = 0.55$ V vs. RHE, the images did not vary, indicating that no significant physical chemical changes occurred under potentiodynamic imaging (Figure 6c).

Figures 7a–c report the STM imaging at different applied potentials of a mixed H$_2$OEP/FeOEP adlayer on HOPG in Ar purged 0.1 M HClO$_4$ electrolyte. The free-base H$_2$OEP molecule was meant to act as an internal standard for the EC-STM imaging study and comparison, since it had already been pointed out its behaviour under the same experimental conditions. In all the three images, the H$_2$OEP molecules can be

recognised basing on their lower height in the extracted topographic profiles. These profiles are comparable to those obtained by the pure H$_2$OEP adlayer in the absence of oxygen.

Conversely, the brighter spots were assigned to FeOEP molecules, whose higher protrusion is justified by the presence of an iron atom in the porphyrin cavity. The starting applied potential (Figure 7a) was $E_{app} = 0.55$ V vs. RHE, as done for pure H$_2$OEP. This potential should be sufficiently positive to maintain the oxidation of iron atoms to (III) oxidation state, as indicated by the Pourbaix diagram.[35] By stepping the potential to $E_{app} = 0.35$ V vs. RHE, the image contrast deeply changes: the protrusions were substituted by enlightened circles enclosing an apparent hole. This particular change occurring at the FeOEP centres coincides with the appearance of a peak in the FeOEP@HOPG voltammetric profile (Figure 3). The most probable physical chemical phenomenon induced by the different polarisation is ascribed to Fe centres reduction from (III) to (II) oxidation state. A new d orbital configuration was then attained, since Fe^{II} features an additional d electron, achieving a d^6 orbital configuration. Therefore, a different behaviour is expected when considering tunnelling events, since a new orbital population was present. To this end, tunnelling parameters were held constant, and the different contrast observed can then justify the occurrence of the Fe reduction. A similar behaviour was already encountered for iron phthalocyanine supported on Au(111).[12]

Let us now take into exam the case of a pure FeOEP adlayer in contact with Ar purged electrolyte. Two high-resolution images are displayed in Figures 7d and e. In both cases, molecules are clearly visible with their cross-like shape. Moreover, a bright sharp spot is visible in the centre of each molecule. Topographic profiles were extracted along the yellow/blue dashed lines. The spots correspond to a protrusion of $\Delta Z \approx 1.5$ Å (Table 2). The presence of iron at the centre of the porphyrins should be reconducted to this additional protrusion with respect to the pure H$_2$OEP layer. In fact, the partially filled d orbital population of the transition metal (iron) is able to
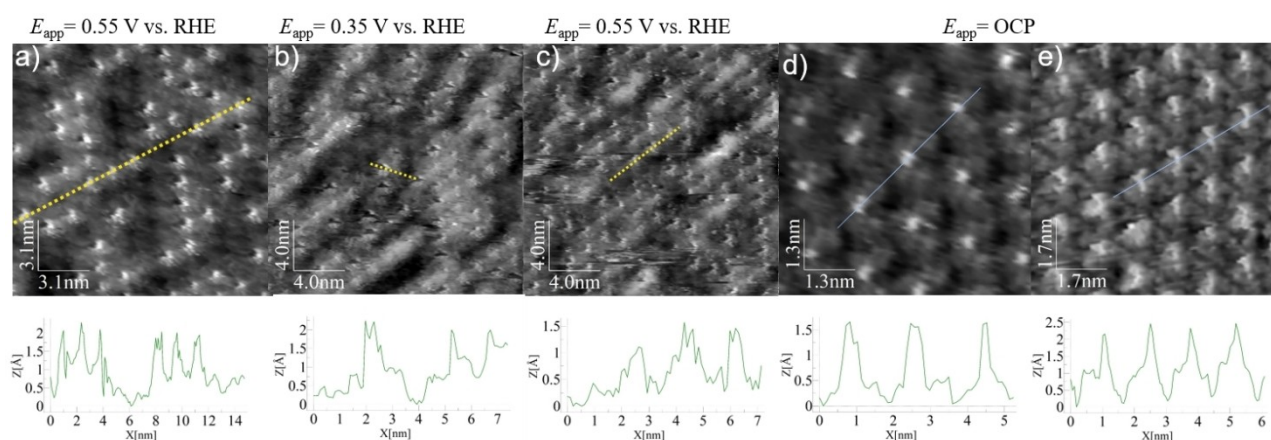

Figure 7. EC-STM in Ar purged 0.1 M HClO$_4$ of (a-c) mix of H$_2$OEP@HOPG and FeOEP@HOPG and (d,e) only FeOEP@HOPG. (a) $I_t = 0.7$ nA; $U_b = -0.450$ V; $E_{app} = 0.550$ V vs. RHE; $I = 0$ μA; (b) $I_t = 0.7$ nA; $U_b = -0.350$ V; $E_{app} = 0.350$ V vs. RHE; $I = -1.5$ μA; (c) $I_t = 0.7$ nA; $U_b = -0.450$ V; $E_{app} = 0.550$ V vs. RHE; $I = 0$ μA; d,e) $I_t = 0.58$ nA; $U_b = -0.450$ V; $E_{app} = $ OCP. The underneath topographic profiles are traced along the yellow dashed line in the corresponding figures.

ChemElectroChem

Articles
doi.org/10.1002/celc.202100543

Chemistry
Europe
European Chemical
Societies Publishing

Table 2. Apparent height of Fe centre of FeOEP and H₂OEP as determined by STM topographic profiles at different applied potentials and electrolyte saturation.

	Ar	Ar	O₂	O₂
H₂OEP	$E = 0.550$ V	$E = 0.250$ V	$E = 0.250$ V	$E = 0.550$[a]
	0.2 Å (dip)	0.2 Å (dip)	0.2 Å (dip)	0.2 Å (dip)
FeOEP	$E = 0.550$ V	$E = 0.350$ V	$E = 0.350$ V	$E = 0.550$ V
	1.5 Å	1 Å (dip)	0.3–0.6 Å	~ 1.5 Å [a]
[a] value uncertain due to the overlap of faradaic noise.				

sustain a higher number of tunnelling events, thereby producing a protrusion in the final STM image.[36,37]

When the electrolyte is saturated with O_2 it is possible to evaluate whether O_2 adsorbs on the iron centre. High-resolution images were achieved, and they are displayed in Figures 8a and b. Both images show the cross-like molecular shape. Moreover, a protrusion is present, but retains some differences with respect to the Ar saturation case. In fact, the spots are more smeared and shifted from the molecular centre.

Another relevant feature stems from the topographic profile comparison. In fact, the measured protrusions are one order of magnitude lower than the Ar saturation case ($\Delta Z_{O_2} \approx 0.3$–0.4 Å). Even if O_2 is an "additional feature" on top of the molecule (two atoms), the result is a reduced protrusion. This is in accordance with what was already observed in literature for the CoOEP behaviour on HOPG.[38] The present system is however more complicated because it accounts for an aqueous electrolyte, and therefore tunnelling is further mediated by water molecules (resonant tunnelling). Indeed, Tersoff-Hamann (TH)[39] simulations of STM maps (not reported), based on DFT results, cannot reproduce the change in the apparent height of the molecule centre. This is most probably related to the limitations of the TH model, which solely relies on the density off states (DOS) of the system.

Two main geometries of adsorption were reported for the Fe—O_2 complex,[40] namely side-on and end-on. They both are predicted as stable; therefore, both can be observed and can be co-present in a single STM image. However, for the shape and contrast revealed in Figure 8a and b, it seems that the end-on geometry was preferred, basing on the consideration that only one O atom is linked to Fe, allowing the O_2 molecule to freely rotate and vibrate (Figure 8c). On the contrary, a side-on bounded O_2 molecule is expected to produce a more symmetrical and less diffused spot.

A mixed adlayer of FeOEP plus H₂OEP was also realised and analysed in O_2 saturated HClO₄ (Figures 8d). This aims to evaluate the selective O_2 adsorption on the Fe centre since imaging of pure H₂OEP adlayer already demonstrated no O_2 adsorption. The STM images showed a difference of contrast among adjacent molecules, indicating the co-presence of the two different molecular systems, as already obtained in the Ar saturation case. Topographic profiles were extracted along the yellow dashed lines, trying to include both darker and brighter molecules. The darker molecules are attributed to H₂OEP, and indeed the insignificant protrusion can be measured, i.e. the profile is rather flat. Brighter molecules are instead ascribed to
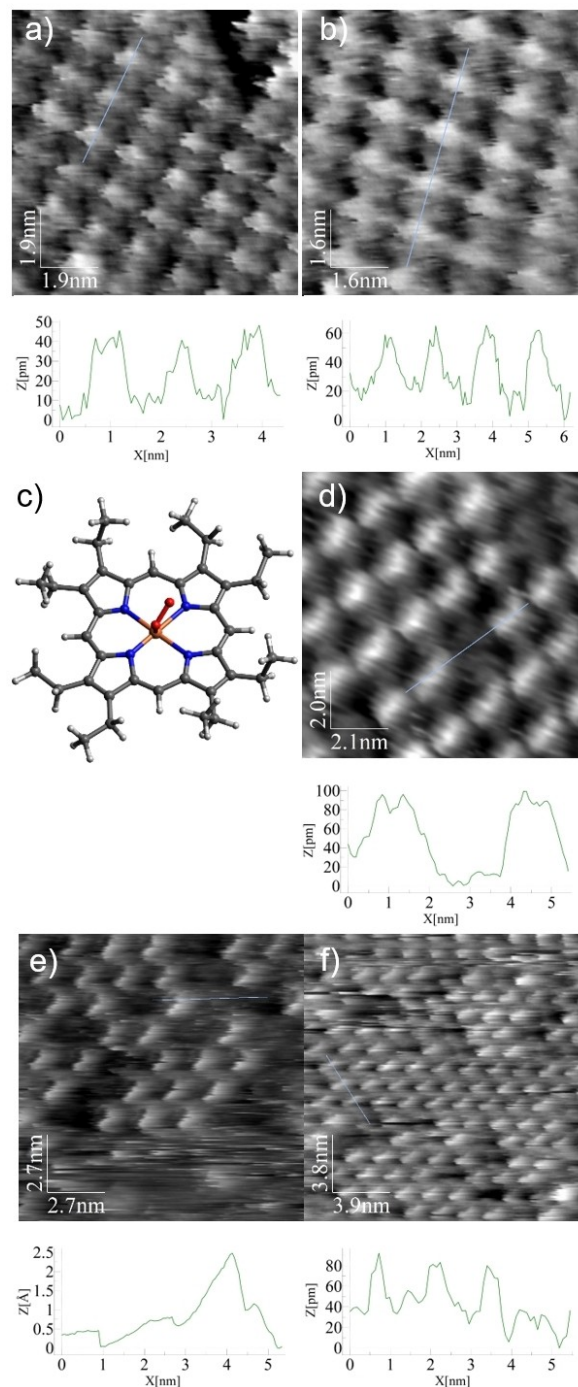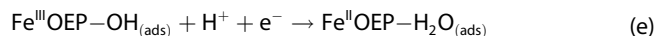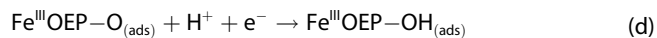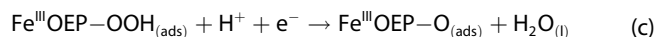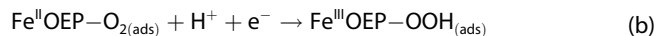

Figure 8. EC-STM in O_2 saturated 0.1 M HClO₄ of (a-b) FeOEP@HOPG $I_t = 0.76$ nA; $U_b = -0.450$ V; $E_{app} = 0.500$ V vs. RHE; $I = 0$ μA; c) Simple model representation of O_2 end-on adsorption on the Fe centre of FeOEP, (d) mix of H₂OEP@HOPG and FeOEP@HOPG $I_t = 1$ nA; $U_b = -0.400$ V; $E_{app} = 0.550$ V vs. RHE; $I = 0$ μA,; e) $I_t = 1$ nA; $U_b = -0.350$ V; $E_{app} = 0.350$ V vs. RHE; $I = -5.2$ μA, f) $I_t = 1$ nA; $U_b = -0.350$ V; $E_{app} = 0.550$ V vs. RHE; $I = 0$ μA. The underneath topographic profiles are traced along the blue line in the corresponding figure.

FeOEP, and the extracted profile has a protrusion of $\Delta Z \approx 0.4$–0.6 Å, which is in accordance with the value obtained in the case of a pure FeOEP adlayer in O_2 saturated electrolyte.

ChemElectroChem

Articles
doi.org/10.1002/celc.202100543

**Chemistry
Europe**
European Chemical
Societies Publishing

Thus, the ability to realise a mixed adlayer of H_2OEP and FeOEP remarkably provides an internal reference, due to the fact that the H_2OEP adlayer does not undergo electrochemical changes, at least for the central spot, while scanning the applied polarisation potential.

The H_2OEP/FeOEP mixed layer was then subjected to potentiodynamic imaging in O_2 saturated electrolyte. At $E_{app} = 0.55$ V vs. RHE, significant differences arise for FeOEP and H_2OEP. FeOEP molecules show the expected profile around 0.5 Å, while H_2OEP are below 0.2 Å, and no spot is visible (Figure 8d). At reductive potential ($E_{app} = 0.35$ V vs. RHE) the Faradaic current contribution is non-negligible and in fact the image quality is worsened (Figure 8e). However, the measured profile seems to show higher protrusions (around 1.5 Å), which were previously ascribed to Fe^{III}. Indeed, at this potential, the Fe centres experience a continuous turn-over due to the ongoing oxygen reduction, making impossible to resolve either O_2 adsorption or the bare Fe atom. Stepping back to 0.55 V vs. RHE (Figure 8f), image quality is restored, and the smeared spots are again clearly visualised, with a protrusion around 0.5 Å.

The ORR was further investigated by estimating the Gibbs free energies $\Delta_r G$ in the reaction pathway. $\Delta_r G$ values were obtained combining DFT calculations, MD outcomes and thermodynamics data. We modelled the catalytic cycle by means of 5 elementary steps:

$$Fe^{II}OEP-H_2O_{(ads)} + O_2 \rightarrow Fe^{II}OEP-O_{2(ads)} + H_2O \quad (a)$$

$$Fe^{II}OEP-O_{2(ads)} + H^+ + e^- \rightarrow Fe^{III}OEP-OOH_{(ads)} \quad (b)$$

$$Fe^{III}OEP-OOH_{(ads)} + H^+ + e^- \rightarrow Fe^{III}OEP-O_{(ads)} + H_2O_{(l)} \quad (c)$$

$$Fe^{III}OEP-O_{(ads)} + H^+ + e^- \rightarrow Fe^{III}OEP-OH_{(ads)} \quad (d)$$

$$Fe^{III}OEP-OH_{(ads)} + H^+ + e^- \rightarrow Fe^{II}OEP-H_2O_{(ads)} \quad (e)$$

A further step, pertaining the formation of hydrogen peroxide, was modelled to verify whether the ORR proceed through a *true* four electrons pathway or through the formation of H_2O_2 and its subsequent reduction ($2 + 2e^-$).

$$Fe^{III}OEP-OOH_{(ads)} + H^+ + e^- \rightarrow Fe^{II}OEP-O_2H_{2(ads)} \quad (f)$$
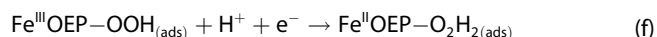
The Gibbs free energy of a reaction is defined as $\Delta_r G = \Delta_r U + \Delta pV - T\Delta_r S$, where Δ_r represents the difference of the pertaining quantity between products and reactants. We evaluated ΔpV using the ideal gas model. Standard entropies of gas-phase O_2 and H_2 and of liquid H_2O were taken from thermodynamic tables,[41] whereas the entropy of adsorbed species was neglected, because entropies of species immobilized on the surface are very small compared to the other species.

The internal energy variation $\Delta_r U$ was obtained as the sum of the variation in ground state energy (E_{GS}) plus the variation in zero-point energy (ZPE). The former was computed as the difference in the DFT total energy between products and reactants computed in vacuum, plus the solvation energy ΔE_{solv} extracted from MD runs. The latter was obtained by

$$\Delta E_{solv} = <E_{all}> - <E_{vacuum}> - <E_{water}> \quad (7)$$

where $<E>$ is the average over the MD snapshots of the total energy, and the labels "all", "vacuum", and "water" stand, respectively, for the whole system graphite+porphyrin+water, the graphite+porphyrin only, and the water box only. Since the same water box was used, the $<E_{water}>$ average is done over the 5 sets of calculations. Thus, it constitutes just a shifting constant to the solvation energy.

Finally, the ZPE values of the adsorbed species were extracted from MD runs using the two-phase thermodynamic method (2PT),[42] while those of molecules in gas- and liquid-phase were taken from literature.[43] In the 2PT method the ZPE is obtained from the vibrational part of the DOS of the system (see eq. 19 of Ref. [42]). The latter is computed from the Fourier transform of the autocorrelation functions of the vibrational velocities, which are obtained by subtracting the roto-translational rigid-body velocities of the molecule from the total velocity of each atom. Since the porphyrin is anchored to the surface, we considered the rotational component to the total velocity negligible.

With these choices, the Gibbs free energy of reaction reads

$$\Delta_r G = \Delta_r E_{DFT} + \Delta_r ZPE + \Delta_r \Delta E_{solv} + \Delta_r pV - T\Delta_r S \quad (8)$$

Moreover, instead of dealing with explicit protons and electrons in equations (b-e), we use as reference the hydrogen molecule and exploit the fact that the Gibbs free energy of the equation

$$H^+ + e^- \rightarrow 1/2H_2 \quad (9)$$

is given by $FV_{SHE} + RT \ln(10) \cdot pH$, where F is the Faraday constant and V_{SHE} is the electrode potential versus the SHE (all the measurements are performed at pH$=1$, thus SHE and RHE matches in value). Therefore, $\Delta_r G$ of equations (b–f) finally reads:

$$\Delta_r G = \Delta_r E_{DFT} + \Delta_r ZPE + \Delta_r \Delta E_{solv} + \Delta_r pV - T\Delta_r S + FV_{SHE} + + RT\ln(10) \cdot pH \quad (10)$$

Results are collected in Table 3. As long as the ORR is carried out in aqueous environment, the first step (a) is described by the adsorption of oxygen at the Fe centre and the concurrent release of a water molecule. This step is predicted to be

Table 3. Energy terms and Gibbs free energies in kJ mol^{-1} of processes described by equations (a-e) and computed accordingly to eqs. 5–6 (see text) in standard conditions: $T = 298$ K, $V_{SHE} = 0$, pH$=0$.

Steps	$\Delta_r E_{DFT}^{PBE+U}$	$\Delta_r \Delta E_{solv}$	$\Delta_r ZPE$	ΔpV	$-T\Delta_r S°$	$\Delta_r G°^{PBE+U}$
a	24.78	−31.48	4.49	−2.48	40.31	35.52
b	−83.96	−13.28	28.10	−1.24	19.48	−50.89
c	−101.35	−41.30	−39.70	−1.24	−1.37	−185.06
d	−189.18	−6.09	25.23	−1.24	19.48	−151.80
e	−123.58	10.55	28.07	−1.24	−1.37	−87.57
f	−92.83	38.63	25.60	−1.24	19.48	−10.36

ChemElectroChem

Articles
doi.org/10.1002/celc.202100543

Chemistry Europe
European Chemical
Societies Publishing

disfavoured in standard conditions. This is probably due to the approximate treatment of the solvation energy, that in this specific case has a relatively important role, being comparable in magnitude to the Gibbs free energy. A better description of solvation is probably needed for this specific step.

All ORR steps are favoured in standard conditions. As observed in many catalytic systems (see e.g.[44]), the least favoured step is the formation of the metastable −OOH species (b), which thus determines the thermodynamic limiting potential of ORR catalysed by FeOEP. In Figure 9 we report the free energy profile of the ORR pathway at pH = 1, matching the value in experiments, using various electrode potential values. It is apparent that the reactions step (b) is favoured for V_{SHE} lower than 0.47 V, that almost coincides with the onset of the reduction peak shown in voltammograms. As apparent from table 3 and figure 9, the Gibbs free energy pertaining the formation of hydrogen peroxide $Fe^{III}OEP−O_2H_2$ (step f) was found to be more positive than the that relative to the formation of the oxo species $Fe^{III}OEP−O$ (step c), which means that the direct 4-electrons mechanism is favoured over the formation of the H_2O_2 intermediate and its subsequent reduction. The plot of such step was reported in figure 9 only for V = 0.0 V vs. SHE, but the energy difference between such step and the concurring one is independent of the electrode potential.

3. Conclusion

Fe(III)-octaethylporphyrin chloride adsorbed on HOPG was studied as molecular probe able to mimic the $Fe−N_4$ single site of Fe−N−C materials in the oxygen reduction reaction, by means of electrochemical scanning tunnelling microscopy, cyclic voltammetry in 0.1 M $HClO_4$ electrolyte and an ab-initio thermodynamics approach. Combining experimental and computational outcomes, a thorough understanding of electrochemical processes happening in this system was reached. The as-deposited monolayer was shown to be composed by FeOEP units. FeOEP in Ar purged 0.1 M $HClO_4$ shows a quasi-reversible reduction peak for the Fe^{III} to Fe^{II} redox process, whereas in O_2 saturated electrolyte a clear irreversible reduction peak was observed at potentials close to the Fe^{III}/Fe^{II} peak potentials and

responsible for a "redox-catalysis like" mechanism. The reduction of the metal centre from (III) to (II) oxidation state is the precondition for the O_2 reduction. RRDE measurement attested the almost tetraelectronic reduction of O_2 to H_2O and Gibbs free energy calculations showed that the four electrons pathway is preferred over the formation of the hydrogen peroxide.

EC-STM potentiodynamic experiments proved that upon the change of the applied potential in Ar purged electrolyte there is a variation of the apparent height of Fe centre of FeOEP attesting the reduction of Fe^{III} to Fe^{II}. Furthermore, in O_2 saturated electrolyte a brighter central spot in FeOEP ($\Delta Z \approx 0.4$–0.6 Å) was associated to the O_2 adsorption on the metal single site and upon the shift of the potential to more negative values there is an evolution of the molecule profile ($\Delta Z \approx 1.5$ Å) confirming the O_2 electroreduction. To strengthen these observations a mixed adlayer of H_2OEP and FeOEP was prepared and characterized, where the non-metallized porphyrin plays as internal reference, which showed to not undergo any potential induced changes, at least for the central spot. However, also $H_2OEP@HOPG$ showed a certain activity for ORR even if far less pronounced than at FeOEP@HOPG, and with a higher selectivity versus H_2O_2. This was explained on the base of pyrrolic functionalities which in carbon doped materials was proved to induce an increased catalytic activity versus the O_2 reduction.

The ORR at FeOEP was further investigated by DFT and MD simulations, by estimating the Gibbs free energies $\Delta_r G$ in the reaction pathway. The catalytic cycle was modelled by means of 5 elementary steps where the least favoured one is the formation of the metastable −OOH species. This step becomes favoured for potentials lower than 0.47 V vs. SHE, that is close to the onset of the reduction peak of FeOEP, as determined by cyclic voltammetry.

Experimental Section

Custom-build EC-STM scanners were employed for EC-STM characterizations. Piezoelectric tubes were purchased by Pi Ceramic. The tube is scratched with a Widia cermet tip, thanks to a dual-micrometre system, obtaining four sectors for the later displacement of the tip, and one sector for its vertical movement. Each sector is electrically insulated by the others. A metallic canula is derived by cutting and refining an insulin needle. A copper wire is crimped within one side of the needle. The canula is glued inside a ceramic tube for electrical insulation, whereas the copper wire is already covered with insulating material, except of the contact with the canula. The ceramic tube is then glued to a brass disk, and the whole system is glued inside the piezoelectric tube, letting the insulated copper wire passing through it. A 0.25 mm straight tungsten wire was subjected to electrochemical etching in 2 M KOH with a square wave AC generator. The obtained tips were rinsed with MilliQ water, and after drying in air they were coated with hot-melt glue (UHU) to create an insulating layer on tungsten, with the aim to prevent Faradaic current at the tip electrode. The very end of the tip is not covered by the hot glue due to its high curvature radius.

For all measurements, perchloric acid solutions were employed. Fluka™ TraceSELECT™ Ultra (Honeywell) perchloric acid was purchased and properly diluted with Millipore Milli-Q water (specific
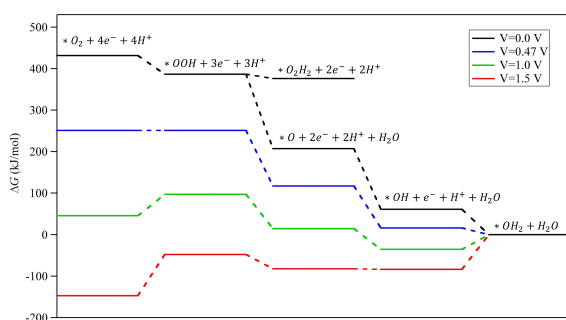

Figure 9. Stability of the intermediates at increasing applied potential V vs. SHE (pH = 1). The formation of the H_2O_2 intermediate was reported only for V = 0 V for sake of clarity.

resistance ≥ 18.2 MΩ cm, TOC ≤ 5 ppb) to reach a concentration of 0.1 M. The obtained solutions were always purged with Ar or saturated with O_2 in order to evaluate the system response in the two cases. A HOPG round-shaped crystal (MaTeck ZYB type dia. 10,00 mm $\times$ thickness/length 2,00 mm mosaic spread $0.8° \pm 0.2°$) was used as the substrate to be functionalised with iron porphyrin molecules. The crystal was always subjected to exfoliation with scotch tape prior to be functionalised and mounted in the electrochemical cell. In this way, a freshly cleaved surface can always be easily obtained.

N,N-Dimethylformamide (HyPerSolv Chromanorm VWR Chemicals) was used to prepare 10^{-4} M solutions of the target molecules. Iron (III) octaethylporphyrin chloride (FeOEP) and free-base octaethyl-porphyrin (H$_2$OEP) were purchased by Sigma-Aldrich and used without any further purification. Three droplets (100 µL) of porphyrin solution were casted on the freshly cleaved HOPG inserted in a weighing bottle, which was closed under Argon atmosphere. After 20 min, the bottle was opened and an Argon stream was directed on the HOPG, letting the drop dry faster. In this way, a properly functionalised surface can be obtained within ca. 60 min. The crystal was then mounted in the PEEK® EC-STM cell and 0.1 M HClO$_4$ was added. Glassware was thoroughly rinsed with Milli-Q water and Piranha solution (1/1 H$_2$SO$_4$/H$_2$O$_2$) before introducing any other liquid. Both EC-STM and CV measurements are referred to Reversible Hydrogen Electrode (RHE). The RHE electrode was freshly prepared before each experiment and consists in a Pt wire mesh sealed to the closed end of a capillary glass tube and refilled with a 0.1 M HClO$_4$ solution from the other open end. H$_2$ was directly electrogenerated at the Pt wire mesh so that half of the Pt mesh was exposed to the H$_2$ bubble confined between the 0.1 M HClO$_4$ solution and the closed end of the capillary.

In the paper, U_b is the bias voltage applied between tip and sample, where the tip is polarized whereas the sample is grounded. U_b can be referred versus the reference electrode (U_b vs. RHE) or versus the working electrode itself, which plays also as sample. E_{app} is the electrode potential applied to the working electrode and it is always refereed to the RHE reference electrode. U_b versus RHE was employed when performing consecutive images at different applied potential (E_{app}), to avoid the change of image contrast or an excessive instrumental noise.

Rotating ring-disc electrode (RRDE, Metrohm; $\varnothing = 5$ mm GC disk and a Pt ring) cyclic and linear sweep voltammetry were carried out in both Ar-purged and O$_2$-saturated 0.5 M H$_2$SO$_4$ solution using an Autolab model 101 N potentiostat. All measurements were done in a glass three-electrode cell thermostated at 25 °C. The RRDE tip was used as working electrode, a platinum wire was used as counter-electrode and a homemade RHE as reference electrode prepared before each experiment. In ORR tests, O$_2$ was bubbled inside the electrolyte solution for at least 30 min. The number of transferred electron (n) was determined by RRDE linear sweep voltammetry (5 mV s^{-1}) according to the following equation (eq. 11):

$$n = \frac{4|i_D|}{|i_D| + |i_R|/N} \tag{11}$$

Where i_D is the current recorded at disk, i_R the current recorded at ring and N the collection efficiency, which is equal to 0.25 as previously determined [5], the ring potential was set to 1.5 V vs. RHE. With the last analysis it is also possible to evaluate the percentage of hydrogen peroxide (eq. 12) produced at the working electrode by rearranging eq. 11:

$$\%_{H_2O_2} = \frac{100(4-n)}{2} = \frac{100 \cdot 2|i_R|}{N \cdot |i_D| + |i_R|} \tag{12}$$

STM images were mainly analysed with WsxM[45] and Gwyddion,[46] applying standard procedures of background subtraction and flattening to gain proper image contrast.

Computational Details

Density Functional Theory (DFT) calculations were carried out using the PWSCF code of Quantum-ESPRESSO (QE).[47] Wavefunctions were expanded on a plane wave basis set with a cut-off of 27 Ry, while the cut-off on electron density was 250 Ry. The interaction between valence electrons and ion cores was described through ultrasoft pseudopotentials.[48] The PBE[49] exchange-correlation functional was employed alongside with the Hubbard correction[50] on the d orbitals of Fe with a U parameter of 3.9 eV.[51] Van der Waals interactions were described through the Grimme dispersion correction,[52] as implemented in QE.[53] Surfaces were modelled using the repeated slab approach, and slab replicas distance was larger than 20 Å in all cases to prevent spurious interactions.

Molecular dynamics (MD) simulations were carried out using the NAMD 2.12 software package.[54] The CHARMM 36[55] force field was employed to parametrize all of the system parts. MD simulations have been carried out for three systems: the water box, the porphyrin+4 layers graphite slab in vacuum, and porphyrin+4 layers graphite slab in water, to estimate the solvation energy (see next Section). Simulations of the whole system in solvent served also for the estimation of the ZPE correction due to the bonding of the small moieties to the porphyrin. All the MD simulations followed the standard protocol: energy minimization (1000 minimization steps), simulated annealing (increments of 1 K from 100 to 298 K, 500 MD steps each temperature) to heat the system to the working temperature, and equilibration and production (10^6 MD steps). Simulations were carried out in the canonical NVT ensemble. The simulation box was prepared to contain a single cell (with a single porphyrin molecule) along the xy-plane, while the z-dimension was sufficiently high (8 nm) to avoid the interaction of the porphyrin with its images due to periodic boundary conditions along the z-axis. Relevant simulation parameters were: 2 fs time step of integration (rigid bonds with H atoms), a Langevin thermostat set at 298.15 K (damping 1 ps), 6 Å cut-off for non-bonded interactions (with switching at 5.5 Å, and pair list distance of 6.5 Å), PME for electrostatics (order 6, tolerance 0.0001). Coordinates were saved each 100 MD steps (0.2 ps), while velocities were dumped each 1 MD step (2 fs) since velocity autocorrelation functions were needed for the evaluation of ZPE (see below).

Conflict of Interest

The authors declare no conflict of interest.

[1] E. Jung, H. Shin, B.-H. Lee, V. Efremov, S. Lee, H. S. Lee, J. Kim, W. Hooch Antink, S. Park, K.-S. Lee, S.-P. Cho, J. S. Yoo, Y.-E. Sung, T. Hyeon, *Nat. Mater.* **2020**, *19*, 436–442.

[2] A. Wang, J. Li, T. Zhang, *Nat. Chem. Rev.* **2018**, *2*, 65–81.

[3] M. Primbs, Y. Sun, A. Roy, D. Malko, A. Mehmood, M.-T. Sougrati, P.-Y. Blanchard, G. Granozzi, T. Kosmala, G. Daniel, P. Atanassov, J. Sharman, C. Durante, A. Kucernak, D. Jones, F. Jaouen, P. Strasser, *Energy Environ. Sci.* **2020**, *13*, 2480–2500.

[4] G. Daniel, T. Kosmala, F. Brombin, M. Mazzucato, A. Facchin, M. C. Dalconi, D. Badocco, P. Pastore, G. Granozzi, C. Durante, *Catalysts* **2021**, *11*, 390–405.

[5] M. Mazzucato, G. Daniel, A. Mehmood, T. Kosmala, G. Granozzi, A. Kucernak, C. Durante, *Appl. Catal. B* **2021**, *291*, 120068–120091.

[6] G. Daniel, T. Kosmala, M. C. Dalconi, L. Nodari, D. Badocco, P. Pastore, A. Lorenzetti, G. Granozzi, C. Durante, *Electrochim. Acta* **2020**, *362*, 137200–137212.

[7] A. Zitolo, V. Goellner, V. Armel, M.-T. Sougrati, T. Mineva, L. Stievano, E. Fonda, F. Jaouen, *Nat. Mater.* **2015**, *14*, 937–942.

[8] I. Matanovic, K. Artyushkova, P. Atanassov, *Curr. Opin. Electrochem.* **2018**, *9*, 137–144.

[9] V. Perazzolo, G. Daniel, R. Brandiele, L. Picelli, G. A. Rizzi, A. A. Isse, C. Durante, *Chem. A Eur. J.* **2021**, *27*, 1002–1014.

[10] G. Daniel, Y. Zhang, S. Lanzalaco, F. Brombin, T. Kosmala, G. Granozzi, A. Wang, E. Brillas, I. Sirés, C. Durante, *ACS Sustainable Chem. Eng.* **2020**, *8*, 14425–14440.

[11] V. Perazzolo, C. Durante, R. Pilot, A. Paduano, J. Zheng, G. A. Rizzi, A. Martucci, G. Granozzi, A. Gennaro, *Carbon* **2015**, *95*, 949–963.

[12] A. Facchin, T. Kosmala, A. Gennaro, C. Durante, *ChemElectroChem* **2020**, *7*, 1431–1437.

[13] Z.-F. Cai, X. Wang, D. Wang, L.-J. Wan, *ChemElectroChem* **2016**, *3*, 2048–2051.

[14] R. Jasinski, *Nature* **1964**, *201*, 1212–1213.

[15] T. M. T. Huynh, T. H. Phan, P. H. Nguyen, K. Wandelt, *Surf. Sci.* **2020**, *694*, 121554.

[16] X. Wang, Z. Cai, Y.-Q. Wang, Y.-C. Feng, H.-J. Yan, D. Wang, L.-J. Wan, *Angew. Chem. Int. Ed.* **2020**, *59*, 16098–16103

[17] J.-Y. Gu, Z.-F. Cai, D. Wang, L.-J. Wan, *ACS Nano* **2016**, *10*, 8746–8750.

[18] X. Qiu, C. Wang, Q. Zeng, B. Xu, S. Yin, H. Wang, S. Xu, C. Bai, *J. Am. Chem. Soc.* **2000**, *122*, 5550–5556.

[19] X. Qiu, C. Wang, S. Yin, Q. Zeng, B. Xu, C. Bai, *J. Phys. Chem. B* **2000**, *104*, 3570–3574.

[20] E. J. Smith, T. Bryk, A. D. J. Haymet, *J. Chem. Phys.* **2005**, *123*, 034706.

[21] T. H. Phan, K. Wandelt, *J. Chem. Phys.* **2015**, *142*, 101917.

[22] J. Maruyama, C. Baier, H. Wolfschmidt, P. Bele, U. Stimming, *Electrochim. Acta* **2012**, *63*, 16–21.

[23] L. Zhang, K. P. Kepp, J. Ulstrup, J. Zhang, *Langmuir* **2018**, *34*, 3610–3618.

[24] Z.-F. Cai, T. Chen, J.-Y. Gu, D. Wang, L.-J. Wan, *Chem. Commun.* **2017**, *53*, 9129–9132.

[25] X. Yin, L. Lin, U. Martinez, P. Zelenay, *ACS Appl. Mater. Interfaces* **2019**, *2*, 7272–7278.

[26] T. Wang, Z.-X. Chen, Y.-G. Chen, L.-J. Yang, X.-D. Yang, J.-Y. Ye, H.-P. Xia, Z.-Y. Zhou, S.-G. Sun, *ACS Energy Lett.* **2018**, *3*, 986–991.

[27] M.-F. Chen, T.-H. Chao, M.-H. Shen, Q. Lu, M.-J. Cheng, *J. Phys. Chem. C* **2020**, *124*, 25675–25685.

[28] Z. Duan, G. Henkelman, *J. Phys. Chem. C* **2020**, *124*, 12016–12023.

[29] K. Takeyasu, M. Furukawa, Y. Shimoyama, S. K. Singh, J. Nakamura, *Angew. Chem.* **2021**, *133*, 5181–5184; *Angew. Chem. Int. Ed.* **2021**, *60*, 5121–5124.

[30] R. Brandiele, F. Poli, L. Picelli, R. Pilot, G. A. Rizzi, F. Soavi, C. Durante, *ChemElectroChem* **2020**, *92*, 455–459.

[31] M. Favaro, L. Ferrighi, G. Fazio, L. Colazzo, C. Di Valentin, C. Durante, F. Sedona, A. Gennaro, S. Agnoli, G. Granozzi, *ACS Catal.* **2015**, *5*, 129–144.

[32] J. Quílez-Bermejo, E. Morallón, D. Cazorla-Amorós, *Carbon* **2020**, *165*, 434–454.

[33] U. Tylus, Q. Jia, K. Strickland, N. Ramaswamy, A. Serov, P. Atanassov, S. Mukerjee, *J. Phys. Chem. C* **2014**, *118*, 8999–9008.

[34] K. Artyushkova, A. Serov, S. Rojas-Carbonell, P. Atanassov, *J. Phys. Chem. C* **2015**, *119*, 25917–25928.

[35] J. H. Zagal, M. T. M. Koper, *Angew. Chem. Int. Ed.* **2016**, *55*, 14510–14521; *Angew. Chem.* **2016**, *128*, 14726–14738.

[36] X. Lu, K. W. Hipps, *J. Phys. Chem. B* **1997**, *101*, 5391–5396.

[37] K. W. Hipps, X. Lu, X. D. Wang, U. Mazur, *J. Phys. Chem.* **1996**, *100*, 11207–11210.

[38] B. A. Friesen, A. Bhattarai, U. Mazur, K. W. Hipps, *J. Am. Chem. Soc.* **2012**, *134*, 14897–14904.

[39] J. Tersoff, D. R. Hamann, *Phys. Rev. B* **1985**, *31*, 805–813.

[40] J. H. Zagal, F. Bedioui, *Electrochemistry of N4 Macrocyclic Metal Complexes*, Springer International Publishing, **2016**.

[41] P. J. Linstrom, W. G. Mallard, *NIST Chemistry Webbook*, National Institute Of Standards and Technology, Gaithersburg MD, **n.d**.

[42] A. Tiwari, C. Honingh, B. Ensing, *J. Chem. Phys.* **2019**, *151*, 244124.

[43] K. K. Irikura, *J. Phys. Chem. Ref. Data* **2007**, *36*, 389–397.

[44] A. Kulkarni, S. Siahrostami, A. Patel, J. K. Nørskov, *Chem. Rev.* **2018**, *118*, 2302–2312.

[45] I. Horcas, R. Fernández, J. M. Gómez-Rodríguez, J. Colchero, J. Gómez-Herrero, A. M. Baro, *Rev. Sci. Instrum.* **2007**, *78*, DOI 10.1063/1.2432410.

[46] D. Nečas, P. Klapetek, *Cent. Eur. J. Phys.* **2012**, *10*, 181–188.

[47] P. Giannozzi, O. Andreussi, T. Brumme, O. Bunau, M. Buongiorno Nardelli, M. Calandra, R. Car, C. Cavazzoni, D. Ceresoli, M. Cococcioni, N. Colonna, I. Carnimeo, A. Dal Corso, S. de Gironcoli, P. Delugas, R. A. DiStasio, A. Ferretti, A. Floris, G. Fratesi, G. Fugallo, R. Gebauer, U. Gerstmann, F. Giustino, T. Gorni, J. Jia, M. Kawamura, H.-Y. Ko, A. Kokalj, E. Küçükbenli, M. Lazzeri, M. Marsili, N. Marzari, F. Mauri, N. L. Nguyen, H.-V. Nguyen, A. Otero-de-la-Roza, L. Paulatto, S. Poncé, D. Rocca, R. Sabatini, B. Santra, M. Schlipf, A. P. Seitsonen, A. Smogunov, I. Timrov, T. Thonhauser, P. Umari, N. Vast, X. Wu, S. Baroni, *J. Phys. Condens. Matter* **2017**, *29*, 465901.

[48] D. Vanderbilt, *Phys. Rev. B* **1990**, *41*, 7892–7895.

[49] J. P. Perdew, K. Burke, M. Ernzerhof, *Phys. Rev. Lett.* **1996**, *77*, 3865–3868.

[50] J. A. Owolabi, M. Y. Onimisi, S. G. Abdu, G. O. Olowomofe, *Comput. Chem.* **2016**, *04*, 73–82.

[51] D. A. Scherlis, M. Cococcioni, P. Sit, N. Marzari, *J. Phys. Chem. B* **2007**, *111*, 7384–7391.

[52] S. Grimme, *J. Comput. Chem.* **2006**, *27*, 1787–1799.

[53] V. Barone, M. Casarin, D. Forrer, M. Pavone, M. Sambi, A. Vittadini, *J. Comput. Chem.* **2009**, *30*, 934–939.

[54] J. C. Phillips, R. Braun, W. Wang, J. Gumbart, E. Tajkhorshid, E. Villa, C. Chipot, R. D. Skeel, L. Kalé, K. Schulten, *J. Comput. Chem.* **2005**, *26*, 1781–1802.

[55] B. R. Brooks, R. E. Bruccoleri, B. D. Olafson, D. J. States, S. Swaminathan, M. Karplus, *J. Comput. Chem.* **1983**, *4*, 187–217.